# Low-angular-momentum General Relativistic Magnetohydrodynamic Accretion Flows around Rotating Black Holes with Shocks

Samik Mitra[ID] and Santabrata Das[ID]
Indian Institute of Technology Guwahati, Guwahati 781039, Assam, India; m.samik@iitg.ac.in, sbdas@iitg.ac.in
*Received 2024 May 7; revised 2024 June 4; accepted 2024 June 6; published 2024 August 2*

## Abstract

We investigate the global structure of the general relativistic magnetohydrodynamic (GRMHD) accretion flows around Kerr black holes containing shock waves, where the disk is threaded by radial and toroidal magnetic fields. We self-consistently solve the GRMHD equations that govern the flow motion inside the disk and for the first time, to our knowledge, we obtain the shock-induced global GRMHD accretion solutions around weakly as well as rapidly rotating black holes for a set of fundamental flow parameters, such as energy ($\mathcal{E}$), angular momentum ($\mathcal{L}$), radial magnetic flux ($\Phi$), and isorotation parameter ($F$). We show that shock properties—namely, the shock radius ($r_{\rm sh}$), compression ratio ($R$), and shock strength ($\Psi$)—strongly depend on $\mathcal{E}$, $\mathcal{L}$, $\Phi$, and $F$. We observe that the shock in the GRMHD flow continues to exist for a wide range of the flow parameters, which allows us to identify the effective domain of the parameter space in the $\mathcal{L}$–$\mathcal{E}$ plane where shock solutions are feasible. Moreover, we examine the modification of the shock parameter space and find that it shifts towards the lower-angular-momentum values with increasing $\Phi$ and black hole spin ($a_{\rm k}$). Finally, we compute the critical radial magnetic flux ($\Phi^{\rm cri}$) that admits shocks in GRMHD flows and ascertain that $\Phi^{\rm cri}$ is higher (lower) for a black hole of spin $a_{\rm k} = 0.99$ (0.0) and vice versa.

*Unified Astronomy Thesaurus concepts:* Accretion (14); Magnetohydrodynamics (1964); Black hole physics (159); Magnetic fields (994); Shocks (2086)

## 1. Introduction

Recent findings of large-scale magnetic fields surrounding supermassive black holes (BHs), as revealed by Event Horizon Telescope Collaboration et al. (2021), indicate their potential influence on the accretion and ejection mechanisms. Earlier, the theoretical proposition of Shakura & Sunyaev (1973) had suggested that angular momentum transport within an accretion disk could be facilitated by magnetohydrodynamical (MHD) turbulence. Almost two decades later, the underlying physical mechanism for angular momentum transport was identified by Balbus & Hawley (1991, 1998), with their seminal work on magnetorotational instability. In reality, an accretion disk around a BH is expected to be threaded by large-scale magnetic fields, which are rooted either from the low-mass companion star or from the interstellar medium (Bisnovatyi-Kogan & Ruzmaikin 1974, 1976; Bisnovatyi-Kogan & Lovelace 2011).

Meanwhile, numerous efforts have been made to understand the nature and structure of the magnetic fields in an accretion flow around a BH (Igumenshchev et al. 2003; Begelman & Pringle 2007; Shafee et al. 2008; Mishra et al. 2016, 2020, and references therein). Based on the geometry of the disk and plasma dynamics surrounding BHs, toroidal magnetic fields appear to be the simplest choice, as indicated by Oda et al. (2007, 2010, 2012), although the plunging region seems to be governed by the poloidal magnetic fields (Hawley 2001; Kato et al. 2004). De Villiers et al. (2003) and Hirose et al. (2004) performed 3D general relativistic MHD (GRMHD) simulations and found that the plunging region is predominantly governed

by poloidal magnetic fields, although ordered toroidal magnetic fields play a significant role in regulating the dynamics of the inner regions of accretion disks. In addition, Avara et al. (2016) numerically showed that in radiatively efficient thin accretion disks, large-scale magnetic fields naturally accrete through the disk, while enhancing the disk's radiative efficiency. Liska et al. (2022) examined the behavior of two-temperature truncated disks using GRMHD simulations and found that the large-scale net poloidal magnetic flux leads to the formation of a two-phase environment, consisting of cold gas clumps moving within a hot magnetically dominated corona. Very recently, Manikantan et al. (2024) performed GRMHD simulations where they initialized the disk with a toroidal magnetic field that dynamically evolved, giving rise to significant poloidal fields via the magnetic dynamo process (Jacquemin-Ide et al. 2024). It is worth mentioning that all these studies are model-dependent and, hence, the exact configuration of the magnetic fields within the disk remains unresolved.

In a magnetized accretion disk, the flow starts accreting subsonically far from the BH. As the flow moves toward a BH, it gains radial velocity, reaching supersonic speeds while crossing the event horizon. Hence, the flow must change its sonic state to become transonic (Fukue 1987; Chakrabarti 1989; Takahashi et al. 1990, 2002), at a radius commonly known as the critical point. Depending on the flow parameters—namely, energy, angular momentum, and the magnetic fields—the flow may contain either single or multiple critical points (MCPs; Sarkar & Das 2016; Das & Sarkar 2018; Sarkar et al. 2018; Mitra et al. 2022). Note that multitransonic flows often exhibit discontinuous shock transitions (Fukue 1987; Chakrabarti 1989; Das et al. 2001; Takahashi et al. 2002). During advection, rotating matter experiences centrifugal repulsion, leading to the accumulation of matter in the vicinity of the BH. This forms a

"virtual" barrier around the BH, triggering the shock transition when possible. Indeed, accretion solutions containing shocks are thermodynamically preferred due to their high entropy content (Becker & Kazanas 2001), which facilitates the explanation of the spectrotemporal signatures of BH X-ray binaries (Chakrabarti & Titarchuk 1995; Mandal & Chakrabarti 2005; Nandi et al. 2012; Iyer et al. 2015; Das et al. 2021; Majumder et al. 2022; Nandi et al. 2024). After realizing the astrophysical significance, shock-induced accretion solutions have been studied both in hydrodynamics (Fukue 1987; Chakrabarti 1989; Yang & Kafatos 1995; Ryu et al. 1997; Lu et al. 1999; Das et al. 2001, 2014, 2009; Becker & Kazanas 2001; Chakrabarti & Das 2004; Fukumura & Tsuruta 2004; Das 2007; Becker et al. 2008; Kumar et al. 2013; Suková & Janiuk 2015; Suková et al. 2017; Aktar et al. 2017; Kim et al. 2019; Dihingia et al. 2019; Sen et al. 2022) as well as MHD (Takahashi et al. 2006; Fukumura et al. 2007, 2016; Sarkar & Das 2015, 2016; Das & Sarkar 2018) scenarios. However, efforts are pending to investigate the accretion dynamics involving shocks in GRMHD flows around rotating BHs.

Motivated by this, we study the MHD accretion flows around Kerr BHs of spin $a_k$ under the GR framework. The GRMHD flow under consideration is characterized by means of the radial magnetic flux ($\Phi$) and isorotation parameter ($F$; McKinney & Gammie 2004), in addition to the flow energy ($\mathcal{E}$) and angular momentum ($\mathcal{L}$). With this, we obtain shock-induced global accretion solutions adopting the relativistic equation of state (REOS; Chattopadhyay & Ryu 2009) for the first time, to the best of our knowledge. We find that shocked solutions exist around both weakly rotating ($a_k \rightarrow 0$) as well rapidly rotating ($a_k = 0.99$) BHs. We examine the shock properties—namely, the shock location ($r_{sh}$), compression ratio ($R$), and shock strength ($\Psi$)—and find that these quantities strongly depend on the model parameters $\mathcal{E}$, $\mathcal{L}$, $\Phi$, and $F$. Moreover, we observe that shocks in the GRMHD flow form continuously for a wide range of model parameters. Hence, we separate the parameter space in the $\mathcal{L}$–$\mathcal{E}$ plane to identify regions where shocked GRMHD solutions are feasible and also examine their modifications with $\Phi$ and $a_k$. We further calculate the critical radial magnetic flux ($\Phi^{cri}$) that admits shock in the GRMHD flow and find that $\Phi^{cri}$ is higher for rapidly rotating BHs compared to nonrotating BHs. Finally, we indicate that the GRMHD shocked accretion flows seem to fail in reaching the magnetically arrested disk (MAD) limit (Igumenshchev et al. 2003; Narayan et al. 2003; Sádowski 2016).

The paper is organized as follows. In Section 2, we describe the GRMHD equations and the underlying model assumptions. In Section 3, we discuss GRMHD shock solutions. In Section 4, we discuss the obtained results. Finally, we summarize the overall findings in Section 5.

## 2. Magnetized Flow: Formalism and Underlying Assumptions

In this paper, we aim to study the magnetized hot accretion flows around a stationary, axisymmetric rotating BH. In Boyer–Lindquist coordinates, the line element of rotating BH spacetime takes the following form (Kerr 1963):

$$ds^2 = -\left(1 - \frac{2r}{\Sigma}\right)dt^2 - \frac{4a_k r}{\Sigma}\sin^2\theta \, dt \, d\phi + \frac{\Sigma}{\Delta}dr^2$$
$$+ \Sigma d\theta^2 + \left[r^2 + a_k^2 + \frac{2ra_k^2}{\Sigma}\sin^2\theta\right]\sin^2\theta d\phi^2, \quad (1)$$

where $\Sigma = r^2 + a_k^2 \cos^2\theta$, $\Delta = r^2 + a_k^2 - 2r$, and $a_k$ is the BH spin. In this work, we express the length $r$ and time $t$ in terms of $r_g$ and $r_g/c$, $r_g = GM_{BH}/c^2$ being the gravitational radius, where $G$ is the gravitational constant, $c$ is the speed of light, and $M_{BH}$ is the mass of the BH. With this unit system, we write the governing GRMHD equations (Lichnerowicz 1970; Anile 1990, and references therein) as

$$\nabla_\mu(\rho u^\mu) = 0; \quad \nabla_\mu T^{\mu\nu} = 0; \quad \nabla_\mu {}^*F^{\mu\nu} = 0, \quad (2)$$

where $\rho$ is the mass density, $u^\mu$ is the four-velocity, $T^{\mu\nu}$ is the energy–momentum tensor, and ${}^*F^{\mu\nu}$ is the dual of Faraday's electromagnetic tensor. We consider an accretion flow with infinite conductivity that allows the magnetic field lines to remain frozen into the accreting plasma according to the ideal GRMHD conditions, i.e., $u_\mu b^\mu = 0$. In a magnetized flow, the energy–momentum tensor is given by (Abramowicz & Fragile 2013)

$$T_\nu^\mu = (T_\nu^\mu)_{Fluid} + (T_\nu^\mu)_{Maxwell}$$
$$= \rho\left(\frac{e + p_{gas} + b^2}{\rho}\right)u^\mu u_\nu + \delta_\nu^\mu\left(p_{gas} + \frac{b^2}{2}\right) - b^\mu b_\nu.$$
$$(3)$$

Here, $p_{gas}$ is the gas pressure, $e$ is the internal energy, $b^\mu$ refers to the four magnetic fields in the comoving frame, and $b^2 = b_\mu b^\mu$. Note that $\delta_\nu^\mu = g^{\mu\alpha}g_{\alpha\nu}$ is the contraction of the covariant and contravariant metric components.

### 2.1. Conserved Quantities in GRMHD Flows

We consider the convergent flow ($u^r < 0$) to be confined in the disk midplane, i.e., $\theta = \pi/2$, and hence the polar component of the four-velocity tends to become zero as $u^\theta \sim 0$. Furthermore, we choose $b^\theta = 0$, making the radial ($b^r$) and toroidal ($b^\phi$) field components independent. With this, we solve the radial behavior of the advective, axisymmetric ($\partial_\phi \rightarrow 0$) flow in the steady state ($\partial_t \rightarrow 0$).

From the particle number conservation equation, we get

$$\sqrt{-g}\,\rho u^r = \text{constant} = C_{\mathcal{M}}, \quad (4)$$

where $C_{\mathcal{M}}$ is a measure of the mass flux and, for a Kerr BH, the determinant $\sqrt{-g} = r^2$ in the $\theta = \pi/2$ limit. Being stationary and axisymmetric, the Kerr metric is associated with two Killing vector fields. As the fluid is assumed to obey the symmetries of the chosen spacetime, the energy–momentum conservation takes the form $\nabla_\mu(T_\nu^\mu \xi^\nu) = 0$, where $\xi^\nu$ refers to the generic Killing vectors. Accordingly, we obtain the globally conserved specific energy flux ($\mathcal{E}$) for $\nu = t$ as

$$-\frac{\sqrt{-g}\,T_t^r}{C_{\mathcal{M}}} = \mathcal{E}, \quad (5)$$

and the conserved specific angular momentum flux ($\mathcal{L}$) is obtained for $\nu = \phi$ as

$$\frac{\sqrt{-g}\,T^r_\phi}{C_\mathcal{M}} = \mathcal{L}. \tag{6}$$

Additionally, the no-monopole constraint (Porth et al. 2019) implies

$$-\sqrt{-g}\,{}^*F^{rt} = \text{const} = \Phi, \tag{7}$$

where ${}^*F^{rt} = u^t b^r - u^r b^t$. The $\phi$-component of the source-free Maxwell equation implies (McKinney & Gammie 2004)

$$\sqrt{-g}\,{}^*F^{r\phi} = \text{const} = F, \tag{8}$$

where ${}^*F^{r\phi} = u^r b^\phi - u^\phi b^r$. It is noteworthy that Equation (8) is commonly known as the relativistic isorotation law. Finally, we obtain the $r$-component of the Navier–Stokes equation by projecting the energy–momentum conservation equation along the radial direction in the fluid frame (Mitra et al. 2022), which is given by

$$\begin{aligned}
&\gamma^r_\mu \nabla_\nu T^{\mu\nu} = 0, \\
&(g^{r\nu} + u^r u^\nu)\nabla_\nu p_{\text{tot}} + \rho h_{\text{tot}} u^\nu \nabla_\nu u^\alpha - \nabla_\nu(b^r b^\nu) \\
&- u^r u_\mu \nabla_\nu(b^\mu b^\nu) = 0,
\end{aligned} \tag{9}$$

where $\gamma^r_\mu\ (=\delta^r_\mu + u^r u_\mu)$ is the projection operator, $p_{\text{tot}}(=p_{\text{gas}} + p_{\text{mag}})$ is the total pressure, $p_{\text{mag}}(=b^2/2)$ is the magnetic pressure, and $h_{\text{tot}}[=(e + p_{\text{gas}})/\rho + b^2/\rho]$ is the total enthalpy.

Following Riffert & Herold (1995) and Peitz & Appl (1997), we calculate the local half-thickness ($H$) of the magnetized disk considering hydrostatic equilibrium in the vertical direction, which is given by

$$H^2 = \frac{p_{\text{gas}} r^3}{\rho \mathcal{F}},\quad \mathcal{F} = \gamma^2_\phi \frac{(r^2 + a^2_k)^2 + 2\Delta a^2_k}{(r^2 + a^2_k)^2 - 2\Delta a^2_k}, \tag{10}$$

where $\gamma_\phi\ (=1/\sqrt{1 - v^2_\phi})$ is the Lorentz factor. We define the specific angular momentum of the flow as $\lambda\ (=-u_\phi/u_t)$, and the angular velocity of the flow is given by $\Omega\ (=u^\phi/u^t)$ (Dihingia et al. 2018; Mitra et al. 2022). We follow Lu (1985) to describe the three components of the fluid velocities in the corotating frame as $v^2_\phi = u^\phi u_\phi/(-u^t u_t)$, $v^2_r = u^r u_r/(-u^t u_t)$, and $v^2_\theta = u^\theta u_\theta/(-u^t u_t)$, where $v_\theta = 0$, as $u^\theta \sim 0$ in the disk midplane. Upon integrating Equation (4), we obtain the globally conserved mass accretion rate in the comoving frame, which is given by

$$\dot{M} = -4\pi \rho v \gamma_v H \sqrt{\Delta}, \tag{11}$$

where $v\ (=\gamma_\phi v_r)$ is the flow velocity and $\gamma_v = 1/\sqrt{1 - v^2}$. In this work, we express the accretion rate as $\dot{m} = \dot{M}/\dot{M}_{\text{Edd}}$, where $\dot{M}_{\text{Edd}}$ is the Eddington accretion rate $(\dot{M}_{\text{Edd}} = 1.4 \times 10^{18}\left(\frac{M_{\text{BH}}}{M_\odot}\right)\text{g s}^{-1}$, $M_\odot$ being the solar mass). In this work, we choose $\dot{m} = 0.001$. Using ideal MHD conditions $u_\mu b^\mu = 0$ and Equations (7)–(8), we express $b^{r,\phi}$ in terms of $\Phi$ and $F$ as

$$b^r = -\frac{\gamma^2_\phi(\Phi + F\lambda)}{u^t \mathcal{A}},\quad b^\phi = \frac{Fv^2 - \gamma^2_\phi(F + \Phi\Omega)}{u^r \mathcal{A}}, \tag{12}$$

where $\mathcal{A} = r^2(v^2 - 1)$. Adopting the transformations in Equation (12), we analyze the magnetized accretion flow in terms of the global constants $\Phi$ and $F$, respectively.

### 2.2. REOS

In order to close the dynamical equations (i.e., Equations (5)–(9) and (11)), we use the REOS (Chattopadhyay & Ryu 2009), which is given by

$$e = \frac{\rho f}{\left(1 + \frac{m_p}{m_e}\right)}, \tag{13}$$

where $m_e$ and $m_p$ are the masses of electrons and ions. The quantity $f$ is expressed in terms of dimensionless temperature ($\Theta = k_B T/m_e c^2$, where $k_B$ is the Boltzmann constant) as

$$f = \left\{1 + \Theta\left(\frac{9\Theta + 3}{3\Theta + 2}\right)\right\} + \left\{\frac{m_p}{m_e} + \Theta\left(\frac{9\Theta m_e + 3m_p}{3\Theta m_e + 2m_p}\right)\right\}. \tag{14}$$

With this, we define the polytropic index as $N = (1/2)(df/d\Theta)$ and the adiabatic index as $\Gamma = 1 + 1/N$. Notably, the characteristic wave speeds for magnetized flows are associated with the Alfvén and magnetosonic waves, respectively. Following Gammie et al. (2003), we define the Alfvén speed as $C^2_a = b_\mu b^\mu/(\rho h_{\text{tot}})$ and the fast-magnetosonic speed as $C^2_f = C^2_s + C^2_a - C^2_s C^2_a$, where the relativistic sound speed is given by $C^2_s = \Gamma p_{\text{gas}}/(e + p_{\text{gas}})$. Moreover, we define the magnetosonic Mach number as $M = v/C_f$.

### 2.3. Critical Point Analysis

We combine Equations (5)–(9) and (11) and obtain three coupled nonlinear differential equations as:

(a) the radial momentum equation:

$$R_0 + R_v \frac{dv}{dr} + R_\Theta \frac{d\Theta}{dr} + R_\lambda \frac{d\lambda}{dr} = 0, \tag{15}$$

(b) the azimuthal momentum equation:

$$\mathcal{L}_0 + \mathcal{L}_v \frac{dv}{dr} + \mathcal{L}_\Theta \frac{d\Theta}{dr} + \mathcal{L}_\lambda \frac{d\lambda}{dr} = 0, \tag{16}$$

(c) the energy equation:

$$\mathcal{E}_0 + \mathcal{E}_v \frac{dv}{dr} + \mathcal{E}_\Theta \frac{d\Theta}{dr} + \mathcal{E}_\lambda \frac{d\lambda}{dr} = 0. \tag{17}$$

The coefficients $(R_j, \mathcal{L}_j, \mathcal{E}_j;\ j \to 0,\ v,\ \Theta,\ \text{and}\ \lambda)$ in Equations (15)–(17) are given in Appendix A.

Using Equations (15)–(17), we obtain the wind equation of the GRMHD flow after some simple algebra as

$$\frac{dv}{dr} = \frac{\mathcal{N}(r, a_k, v, \Theta, \lambda, \Phi, F)}{\mathcal{D}(r, a_k, v, \Theta, \lambda, \Phi, F)}, \tag{18}$$

where the explicit expression of the numerator $\mathcal{N}$ and denominator $\mathcal{D}$ are given in Appendix B. Moreover, we express the gradients of the angular momentum ($\lambda$) and

temperature ($\Theta$) in terms of $dv/dr$ as

$$\frac{d\lambda}{dr} = \frac{\mathcal{L}_\Theta \mathcal{E}_0 - \mathcal{L}_0 \mathcal{E}_\Theta}{\mathcal{L}_\lambda \mathcal{E}_\Theta - \mathcal{L}_\Theta \mathcal{E}_\lambda} + \frac{(\mathcal{L}_\Theta \mathcal{E}_v - \mathcal{L}_v \mathcal{E}_\Theta)}{\mathcal{L}_\lambda \mathcal{E}_\Theta - \mathcal{L}_\Theta \mathcal{E}_\lambda} \frac{dv}{dr}, \qquad (19)$$

and

$$\frac{d\Theta}{dr} = \frac{\mathcal{L}_\lambda \mathcal{E}_0 - \mathcal{L}_0 \mathcal{E}_\lambda}{\mathcal{L}_\Theta \mathcal{E}_\lambda - \mathcal{L}_\lambda \mathcal{E}_\Theta} + \frac{(\mathcal{L}_\lambda \mathcal{E}_v - \mathcal{L}_v \mathcal{E}_\lambda)}{\mathcal{L}_\Theta \mathcal{E}_\lambda - \mathcal{L}_\lambda \mathcal{E}_\Theta} \frac{dv}{dr}. \qquad (20)$$

In order to obtain GRMHD accretion solutions around a rotating BH, we simultaneously solve Equations (18)–(20) for a set of model parameters—namely, $\mathcal{E}$, $\mathcal{L}$, $\Phi$, $F$, and $a_k$, respectively.

Usually, the accreting matter begins its journey from the outer edge ($r_{\rm edge}$) of the disk with subsonic radial velocity ($v \ll 1$) and descends into the BH supersonically ($v \sim 1$) to fulfill the inner boundary conditions imposed by the horizon. Therefore, the flow must become transmagnetosonic at least once, if not more, while passing through the critical point ($r_c$). At the critical point, the wind equation (Equation (18)) takes an indeterminate form as $(dv/dr)|_{r_c} = 0/0$, which yields the critical point conditions $\mathcal{N} = \mathcal{D} = 0$. However, in reality, a convergent flow always remains smooth along the streamlines, even while passing through $r_c$. Hence, the velocity gradient must be real and finite everywhere. We, therefore, imply l'Hôpital rule in Equation (18) to evaluate the velocity gradient at $r_c$. Accordingly, we obtain two unique values of $(dv/dr)|_{r_c}$; one of them relates to accretion, and the other one is for wind. When both $(dv/dr)|_{r_c}$ values are real and opposite in sign, a saddle-type critical point is formed (Das 2007; Das et al. 2022; Mitra et al. 2022, 2023). Such points have special significance, as transmagnetosonic solutions can only pass through these points before entering into the BH. Depending on the model parameters, when the critical point forms close to the horizon, it is named as the inner ($r_{\rm in}$) critical point, whereas the outer one ($r_{\rm out}$) is formed far away from the horizon. Notably, the GRMHD accretion flow around BHs often possesses MCPs, depending on the model parameters ($a_k$, $\mathcal{E}$, $\mathcal{L}$, $\Phi$, $F$). Such GRMHD flows are potentially viable for harboring shock waves (Fukue 1987; Chakrabarti 1989; Das & Chakrabarti 2004; Das 2007; Dihingia et al. 2019; Das et al. 2022, and references therein). Accordingly, in the subsequent sections, we study the shock-induced magnetized accretion flows around a rotating BH adopting the GR framework.

### 3. Shock-induced GRMHD Accretion Flow

Depending on the model parameters ($a_k$, $\mathcal{E}$, $\mathcal{L}$, $\Phi$, $F$), the GRMHD flow becomes supersonic after passing through the outer critical point ($r_{\rm out}$) and continues to proceed toward the BH. Meanwhile, the flow starts experiencing centrifugal repulsion, which momentarily slows down the accreting matter. Because of this, matter accumulates in the vicinity of the BH, and a barrier is formed in the form of an effective boundary layer around the BH. Such a centrifugal barrier cannot hold the accumulation of matter indefinitely and beyond a critical limit, so it eventually triggers the discontinuous transition of the flow variables in the form of shock waves (Fukue 1987; Chakrabarti 1989; Frank et al. 2002; Takahashi et al. 2002; Das & Chakrabarti 2007; Fukumura et al. 2007; Sarkar & Das 2016; Sarkar et al. 2018; Dihingia et al. 2019, 2020). Considering this, we describe the shock conditions for the MHD flow in the GR framework below, which eventually

enable us to study the shock properties—namely, the shock location ($r_{\rm sh}$), shock compression ratio ($R$), and shock strength ($\Psi$).

In order to execute a discontinuous shock transition, the magnetized accretion flow must satisfy the GR shock conditions (Lichnerowicz 1970; Appl & Camenzind 1988; Takahashi et al. 2006; Fukumura et al. 2007), which are given by:

(a) Mass flux conservation: $[\rho u^r] = 0$.

(b) Energy flux conservation: $\left[ \frac{T^r_t}{\rho u^r} \right] = 0$.

(c) Angular momentum flux conservation: $\left[ \frac{T^r_\phi}{\rho u^r} \right] = 0$.

(d) Radial magnetic flux conservation: $[^*F^{rt}] = 0$.

(e) Isorotation conservation: $[^*F^{r\phi}] = 0$.

(f) Pressure balance condition: $\left[ \frac{T^{rr}}{\rho u^r} \right] = 0$.

Here, the square bracket "[]" denotes the difference of a quantity across the shock front. Using these conditions, we obtain a shock-induced global GRMHD accretion solution around a rotating BH. Note that in this work, we assume the shocks to be thin and nondissipative in nature, for simplicity.

Across the shock front ($r_{\rm sh}$), the supersonic preshock flow jumps into the subsonic branch, resulting in a hot and dense postshock flow (equivalently, postshock corona; hereafter, PSC; Aktar et al. 2015). This happens because the kinetic energy of the preshock flow is converted into thermal energy and the postshock flow becomes compressed due to shock compression. This yields the PSC to act as a perfect reservoir of hot electrons, which eventually intercepts the soft photons from the cooler preshock flow and reprocesses them to produce high-energy radiation via inverse Comptonization (Chakrabarti & Titarchuk 1995). After the shock transition, the subsonic flow gradually gains its radial velocity and ultimately enters into the BH supersonically, after crossing the inner critical point ($r_{\rm in}$).

### 4. Results

We investigate the dynamical structure of shock-induced transmagnetosonic accretion solutions around a BH of spin $a_k$ for a set of model parameters—namely $\mathcal{E}$, $\mathcal{L}$, $\Phi$, and $F$, respectively. In doing so, we examine the effects of the radial magnetic flux ($\Phi$) and isorotation parameter ($F$) on the GRMHD solutions. Given the diminutive nature of the dimensionless radial magnetic flux and isorotation parameter, we denote them as $\Phi = \Phi_{13} \times 10^{-13}$ and $F = F_{15} \times 10^{-15}$, maintaining the notation $\Phi_{13}$ and $F_{15}$ to signify magnetic flux values. Moreover, in this work, we choose $M_{\rm BH} = 10 M_\odot$ and $\dot{m} = 0.001$ as fiducial values, unless stated otherwise.

#### 4.1. Shock-induced Global GRMHD Accretion Solutions

To begin with, we consider an advective flow that accretes toward a nonrotating BH starting from the outer edge of the disk at $r_{\rm edge} = 1000$. The flow is characterized with the model parameters as $\mathcal{E} = 1.001$, $\mathcal{L} = 3.15$, $F_{15} = 7.5$, and $a_k = 0$. The obtained results are plotted in Figure 1(a), where a fast-magnetosonic Mach number ($M = v/C_f$) is plotted with radial coordinate ($r$) for accretion solutions containing shock waves. Here, we observe that for $\Phi_{13} = 0.0$, the subsonic flow changes its sonic state after crossing the outer critical point at $r_{\rm out} = 302.235$, to become supersonic. While the supersonic flow can smoothly enter into the BH (thin dashed curve), it undergoes
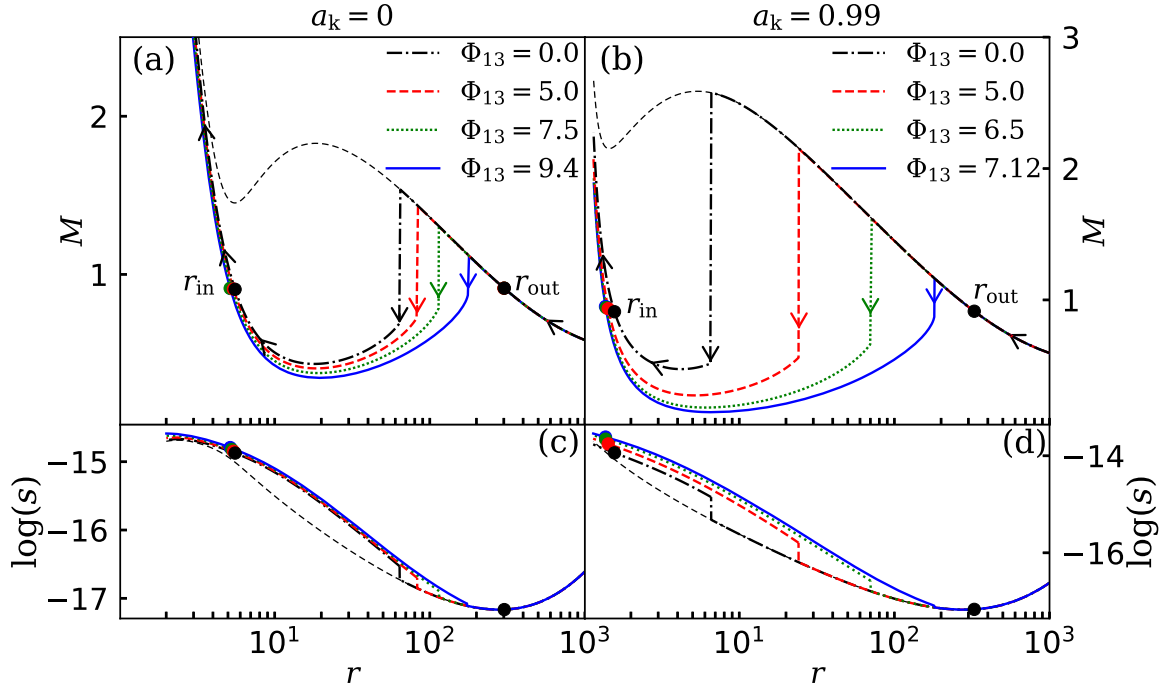
**Figure 1.** Plot of fast-magnetosonic Mach number ($M = v/C_f$) with radial coordinate ($r$) for shock-induced accretion solutions around BHs. The chosen model parameters are $(\mathcal{E}, F_{15}) = (1.001, 7.5)$. (a) The dotted–dashed, dashed, dotted, and solid curves denote the accretion solutions for $\Phi_{13} = 0.0, 5.0, 7.5$, and $9.4$, respectively, where $\mathcal{L} = 3.15$ and $a_k = 0.0$. (b) The dotted–dashed, dashed, dotted, and solid curves denote the accretion solutions for $\Phi_{13} = 0.0, 5.0, 6.5$, and $7.12$, respectively, where $\mathcal{L} = 1.95$ and $a_k = 0.99$. In both panels, the vertical arrows indicate the shock transitions at radii ($r_{sh}$) and the filled circles denote the critical points ($r_{in}$ and $r_{out}$). The arrows indicate the overall direction of the flow motion toward the BH. The entropy densities ($s$) associated with the solutions presented in (a) and (b) are presented in (c) and (d), respectively. See the text for details.

a discontinuous shock transition at $r_{sh} = 63.881$ (dotted–dashed vertical arrow), as the entropy content of the postshock branch is higher compared to the preshock flow (Das et al. 2001). This is not surprising, as it happens in accordance with the second law of thermodynamics, due to the fact that the shocked solution is thermodynamically preferred (Becker & Kazanas 2001) over the shock-free solution. After the shock, the subsonic flow gradually gains radial velocity as it moves inward and crosses the inner critical point at $r_{in} = 5.556$, before entering the BH super-sonically. This result is presented using the dotted–dashed (blue) curve. Next, we increase the radial magnetic flux as $\Phi_{13} = 5.0$, keeping the other model parameters fixed, which increases the magnetic pressure, leading to the rise of the total pressure ($p_{tot}$). This eventually pushes the shock front outward and the shock settles down to a larger radius at $r_{sh} = 83.088$. This result is shown using the dashed (red) curves, and the dashed vertical arrow denotes the location of the shock transition. For a further increase of the radial magnetic flux as $\Phi_{13} = 7.5$, the shock transition happens at $r_{sh} = 113.975$ and the shock-induced GRMHD solution is depicted using a dotted (green) curve. Needless to mention, an indefinite increase of $\Phi_{13}$ is not possible, because, beyond a critical limit of radial magnetic flux $\Phi_{13} = 9.4$, the shock ceases to exist as the shock conditions (Section 3) are not satisfied. In the figure, we denote this solution using the solid (blue) curve. Furthermore, following Das et al. (2009), Porth et al. (2017), and Mitra et al. (2022), we compute the specific entropy function ($s \propto p_{tot}/\rho^{\Gamma-1}$) corresponding to the shocked accretion solutions delineated in Figure 1(a) and plot it as a function of $r$ in panel Figure 1(c). We observe that in all cases, $s$ jumps to a higher value at the shock radius ($r_{sh}$), which evidently confirms that shocked accretion solutions possess higher entropy than the shock-free solution.

We continue to examine the effect of $\Phi_{13}$ on the flow solutions for a rapidly rotating BH as well. Toward this, we choose $a_k = 0.99$ and keep the remaining model parameters unchanged (i.e., $\mathcal{E} = 1.001$ and $F_{15} = 7.5$), as in Figure 1(a), except we use $\mathcal{L} = 1.95$ to obtain the shock-induced magnetized accretion solutions. The obtained results are shown in Figure 1(b). Note that we use a lower $\mathcal{L}$ value for higher $a_k$ simply because a low-angular-momentum flow ($\mathcal{L}$) can only sustain shocks around rapidly rotating BHs (Dihingia et al. 2019; Sen et al. 2022). We observe that for $\Phi_{13} = 0$, the shock transition happens at a relatively smaller radius, at $r_{sh} = 6.525$ (denoted by the dotted–dashed vertical arrow), compared to the nonspinning case. This seems to happen as the lower $\mathcal{L}$ resulted in weak centrifugal repulsion and, hence, the shock front moves farther inward. However, when $\Phi_{13}$ is increased to 5.0, 6.5, and 7.0, the shock front moves outward as expected, and we obtain $r_{sh} = 24.25$ (dashed in red), 70.07 (dotted in green), and 180.74 (solid in blue), respectively. Note that beyond $\Phi_{13} = 7.12$, the shock conditions are not favorable and, hence, the shock transition ceases to exist for the chosen set of model parameters. We further notice that the Mach number ($M$) of the relativistic magnetized flow generally remains restricted as $M \geqslant 3$ around a rapidly spinning BH, mainly due to the rapid increase in sound speed close to the horizon. This happens because of the frame-dragging effect (Fukumura & Kazanas 2007) around a rotating BH. Here, the rotation of the BH compels matter to corotate with the BH along the $\phi$-direction, before getting trapped by the strong gravitational pull. This essentially heats up the inner disk and, hence, the sound speed increases. Indeed, a similar finding is observed for GR hydrodynamic flows as well (Dihingia et al. 2018). Next, in Figure 1(d), we present the plot of the specific entropy function
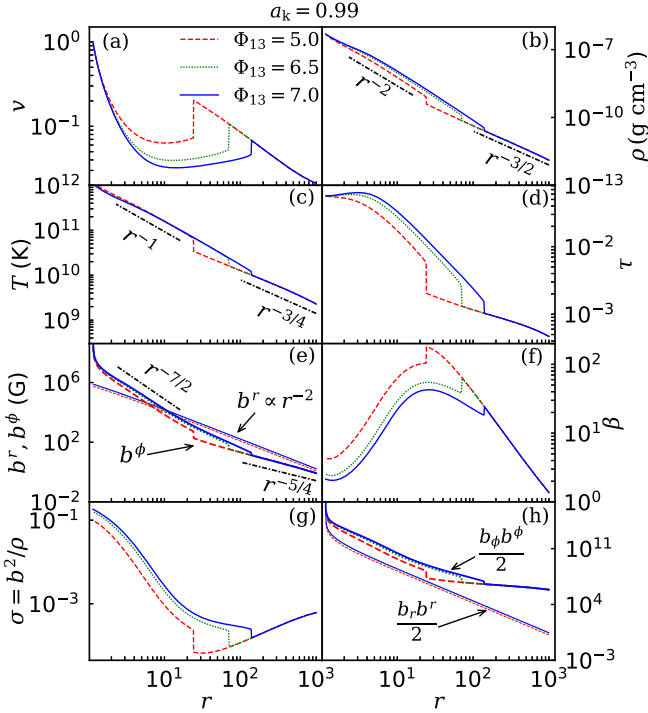
**Figure 2.** Radial variation of the primitive flow variables corresponding to the shock-induced GRMHD accretion solutions presented in Figure 1(b). In panels (a)–(h), profiles of radial velocity ($v$), density ($\rho$), temperature ($T$), scattering optical depth ($\tau$), radial ($b^r$) and toroidal ($b^\phi$) magnetic fields, plasma-$\beta$, magnetization ($\sigma = b^2/\rho$), and radial and toroidal magnetic pressures are plotted for different $\Phi_{13}$. The dashed (red), dotted (green), and solid (blue) curves denote the results for $\Phi_{13} = 5.0$, 6.5, and 7.12, respectively. In panels (b), (c), and (e), the dotted–dashed lines represent best-fit power-law profiles of pre- and postshock flow variables. See the text for details.

($s$) with $r$ for the solutions presented in Figure 1(b), and find that for all instances, $s$ undergoes a significant increase at $r_{sh}$. This provides clear evidence that shocked accretion solutions possess higher entropy compared to the solution without a shock.

### 4.2. Flow Variables of Shock-induced GRMHD Accretion Solutions

In Figure 2, we investigate the behavior of various flow variables corresponding to the shocked GRMHD solutions depicted in Figure 1. In Figure 2(a), we present the radial velocity ($v$) variation as a function of $r$ around a rapidly rotating BH of spin $a_k = 0.99$. We observe that for a set of model parameters $\mathcal{E} = 1.001$, $\mathcal{L} = 1.95$, and $F_{15} = 7.5$, the flow velocity monotonically increases in the preshock region and discontinuously drops down to the subsonic branch at the shock radius $r_{sh}$. After the shock transition, the flow momentarily slows down, although it gradually picks up radial velocity and ultimately enters into the BH with a velocity comparable to the speed of light ($c$). The results plotted using the dashed (red), dotted (green), and solid (blue) lines are obtained for $\Phi_{13} = 5.0$, 6.5, and 7.12, respectively, which are marked in the figure, and vertical lines denote the shock transition radii. In Figure 2(b), we show the variation of mass density ($\rho$) with $r$, where a sudden increase in $\rho$ is observed just after the shock transition for all $\Phi_{13}$ values. This happens because the radial velocity decreases at the shock and, hence, $\rho$ increases to a higher value in order to preserve the conservation

of mass flux across the shock front. We observe that the postshock density profile follows a steeper power law as $\rho \propto r^{-2}$, whereas the preshock density follows $\rho \propto r^{-3/2}$. Note that the preshock density profile exactly matches with the self-similar solutions for a pure inflow model in the absence of outflows (Narayan & Yi 1995). In Figure 2(c), we depict the variation of the flow temperature ($T$) with $r$. During the shock transition, the supersonic flow jumps into the subsonic branch and loses most of its kinetic energy, which results in a hot postshock flow. We notice that the temperature profile follows $T \propto r^{-1}$, which is commonly observed in radiatively inefficient accretion flow simulations (Chatterjee et al. 2023; Olivares et al. 2023). However, in the preshock regime, the flow maintains a relatively shallower profile as $T \propto r^{-3/4}$. Due to shock compression, the hot and dense postshock flow becomes puffed up, resulting in an effective boundary layer (PSC) surrounding the BH. The presence of such a coronal structure significantly affects the emergent radiation from the disk (Chakrabarti & Titarchuk 1995; Poutanen 1998; Nandi et al. 2012, and references therein). Keeping this in mind, in Figure 2(d), we estimate the scattering optical depth $\tau = \kappa \rho H$, where $\kappa$ ($= 0.38 \, \mathrm{cm^2 \, g^{-1}}$) is the electron scattering opacity and $H$ is the disk half-thickness. We find that the disk continues to remain optically thin ($\tau < 1$) in the postshock regime, which eventually indicates that the emergent high-energy radiation can easily escape from the PSC. Next, in Figure 2(e), we show the variation of the radial ($b^r$; thin lines) and toroidal ($b^\phi$; thick lines) magnetic fields as a function of $r$. We notice that $b^r$ increases monotonically with decreasing $r$, following the $b^r \propto r^{-2}$ profile. We also observe that in the preshock regime, the toroidal field follows a self-similar profile, as $b^\phi \propto r^{-5/4}$, and it is amplified at $r_{sh}$ just to maintain the continuity of radial flux ($\Phi_- = \Phi_+$) across the shock front. Thereafter, $b^\phi$ continues to follow a steeper power law, as $b^\phi \propto r^{-7/2}$. With this, the toroidal magnetic field reaches up to $\sim 10^{7-9}$ Gauss near the horizon for the chosen accretion solutions, where magnetic activities are strongest. However, the radial magnetic field limits itself within $\sim 10^{5-6}$ Gauss. An equivalent assessment of magnetic activity is illustrated with the variation of plasma $-\beta$ ($= p_{gas}/p_{mag}$) in Figure 2(f). As the flow starts accreting toward the BH, gas pressure ($p_{gas}$) initially dominates over the magnetic pressure ($p_{mag}$), which enhances $\beta$ values. Indeed, $\beta$ decreases at the PSC as $b^\phi$ jumps up higher and it yields a magnetically stronger PSC, although the flow remains thermal-pressure-dominated ($\beta > 1$). We further notice that the magnetization $\sigma$ ($= b^2/\rho$) varies with $r$, as shown in Figure 2(g), and $\sigma$ becomes roughly $\sim 100$ times higher near the horizon as compared to the outer-edge value. Finally, we present the variation of the magnetic pressure corresponding to the radial and toroidal components and find that the toroidal magnetic pressure dominates the disk MHD as $b^\phi b_\phi > b_r b^r$ all throughout the disk, including near the horizon domain (see Figure 2(h)).

It is useful to examine the properties of the primitive flow variables focusing on a nonrotating BH ($a_k = 0.0$), as illustrated in Figure 3. The model parameters remain consistent with those in Figure 2, except for $\mathcal{L} = 3.15$. The radial variations of the flow variables exhibit qualitative similarity with the results obtained for solutions around a rapidly rotating BH of spin $a_k = 0.99$. Nevertheless, as the shock transition tends to occur at relatively larger radii around a nonrotating BH ($a_k = 0.0$), the compression at the postshock flow weakens. As a result, the
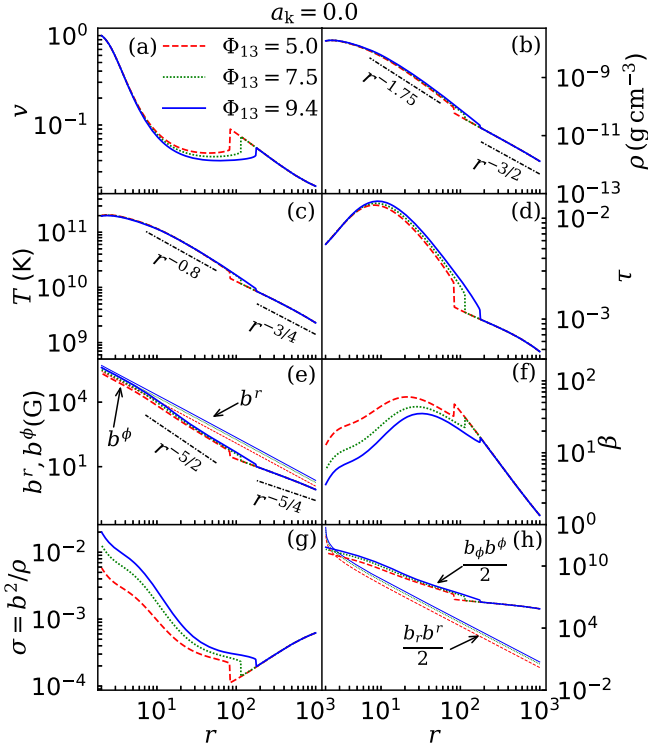
**Figure 3.** The same as Figure 2, but the flow variables correspond to the shocked solutions presented in Figure 1(a). Here, the dashed (red), dotted (green), and solid (blue) curves denote the results for $\Phi_{13} = 5.0$, 7.0, and 9.4, respectively. See the text for details.
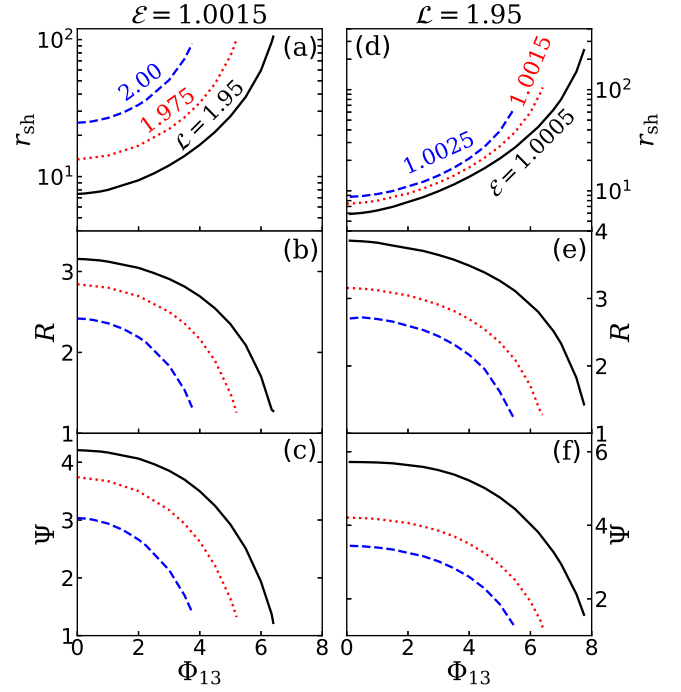


**Figure 4.** Variation of shock location $r_{\rm sh}$ ((a) and (d)), compression ratio $R$ ((b) and (e)), and shock strength $\Psi$ ((c) and (f)) with $\Phi_{13}$. In the left panels, the angular momentum flux is varied as $\mathcal{L} = 1.95$, 1.975, and 2.00, keeping $\mathcal{E} = 1.0015$ fixed. Similarly, in the right panels, we vary the energy as $\mathcal{E} = 1.0005$, 1.0015, and 1.0025 for fixed $\mathcal{L} = 1.95$. The remaining model parameters are set as $a_{\rm k} = 0.99$ and $F_{15} = 5.0$. See the main text for details.

density ($\rho$), temperature ($T$), and magnetic fields near the BH decrease. This results in shallower fitting profiles of the postshock flow variables in panel (b) $\rho \propto r^{-1.75}$, (c) $T \propto r^{-0.8}$, and (e) $b^\phi \propto r^{-5/2}$, compared to the results obtained for $a_{\rm k} = 0.99$. Notably, the preshock variables exhibit the same radial dependency as observed in Figure 2, regardless of the spin of the BH. Finally, it is observed that the radial component of magnetic pressure ($b^r b_r/2$) exceeds the toroidal component ($b^\phi b_\phi/2$) near the horizon (as shown in Figure 3(h)), which contrasts with the rotating BH case (as shown in Figure 2(h)).

### 4.3. Shock Properties

It is intriguing to investigate the effect of magnetic fields on the shock properties—namely, the shock location ($r_{\rm sh}$), compression ratio ($R$), and shock strength ($\Psi$)—as the spectral properties of the BH often rely on these quantities (Chakrabarti & Titarchuk 1995; Nandi et al. 2012, 2018). Toward this, we examine how the shock properties change with the radial magnetic flux ($\Phi_{13}$) and isorotation parameter ($F_{15}$) for GRMHD flows accreting onto a rapidly rotating BH of spin $a_{\rm k} = 0.99$.

In Figure 4(a), we depict the variation of the shock location ($r_{\rm sh}$) as a function of radial magnetic flux ($\Phi_{13}$) for different values of angular momentum ($\mathcal{L}$). Here, we choose $\mathcal{E} = 1.0015$ and $F_{15} = 5.0$. The solid, dotted, and dashed curves represent the results for $\mathcal{L} = 1.95$, 1.975, and 2.0, respectively. We observe that for the chosen set of model parameters ($\mathcal{E}, \mathcal{L}, F_{15}$), standing shocks form for the minimum radial flux limit $\Phi_{13}^{\rm min} = 0$. Moreover, we find that for a fixed $\mathcal{L}$, standing shocks continue to form at larger radii, as $\Phi_{13}$ is increased until it reaches a critical limit ($\Phi_{13}^{\rm cri}$). Beyond $\Phi_{13}^{\rm cri}$, the shock

disappears as the shock conditions are not satisfied. Indeed, $\Phi_{13}^{\rm cri}$ does not possess a universal value, as it depends on the other model parameters. Further, we notice that for fixed $\Phi_{13}$, shocks form at larger radii as $\mathcal{L}$ is increased. This evidently indicates that standing shocks in GRMHD flows seem to be centrifugally supported. Indeed, it is useful to study the density profile of the GRMHD flow, as the emitted radiation directly depends on it. Meanwhile, we find that a convergent GRMHD flow experiences density compression across the shock front $r_{\rm sh}$ (see Figures 2(b) and 3(b)). Accordingly, we compute the compression ratio $R$, defined as the ratio of surface mass density ($\Sigma = \rho H$) of the postshock and preshock flows, and depict it in Figure 4(b) as a function of $\Phi_{13}$ for the same set of model parameters as in Figure 4(a). For a fixed $\mathcal{L}$, $R$ decreases with higher $\Phi_{13}$. This happens because enhanced $\Phi_{13}$ increases the magnetic pressure inside the disk and, hence, the shock front is pushed outward, resulting in the weakening of the density compression due to the expansion of the PSC size. Similarly, for a given $\Phi_{13}$, a GRMHD flow with higher $\mathcal{L}$ experiences less compression at the PSC as increased centrifugal pressure counteracts the inward motion of the flow. Overall, we observe that a strong shock ($R \rightarrow 4$) exists for smaller $\Phi_{13}$, whereas the shock tends to become weak ($R \rightarrow 1$) for larger $\Phi_{13}$. We further compute the shock strength ($\Psi$) that accounts for the temperature jump across the shock front. The shock strength is defined as the ratio of the preshock to postshock Mach numbers, as $\Psi = \frac{v_- / C_{s-}}{v_+ / C_{s+}}$, and we plot $\Psi$ in Figure 4(c) as a function of $\Phi_{13}$ for identical model parameters, as in Figure 4(a). We find that for a given $\mathcal{L}$, $\Psi$ is stronger when $\Phi_{13}$ is smaller and vice versa. Moreover, we observe that $\Psi$ exhibits a similar trend to that of the compression ratio ($R$).
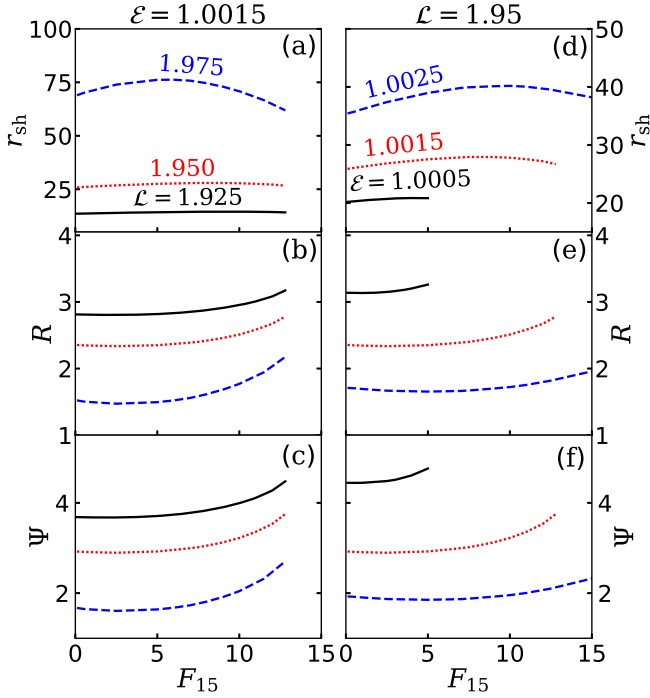
**Figure 5.** Variation of shock location $r_{\rm sh}$ ((a) and (d)), compression ratio $R$ ((b) and (e)), and shock strength $\Psi$ ((c) and (f)) with $F_{15}$. In the left panels, the angular momentum flux is varied as $\mathcal{L} = 1.925$, $1.950$, and $1.975$, keeping $\mathcal{E} = 1.0015$ fixed. Similarly, in the right panels, we vary the energy as $\mathcal{E} = 1.0005$, $1.0015$, and $1.0025$ for fixed $\mathcal{L} = 1.95$. The remaining model parameters are set as $a_{\rm k} = 0.99$ and $\Phi_{13} = 5.0$. See the text for details.

In Figure 4(d), we show the variation $r_{\rm sh}$ with $\Phi_{13}$ for different values of flow energy ($\mathcal{E}$). Here, we choose $\mathcal{L} = 1.95$ and $F_{15} = 5.0$. The solid, dotted, and dashed curves denote the results corresponding to $\mathcal{E} = 1.0005$, $1.0015$, and $1.0025$, respectively. We find that for a fixed $\mathcal{E}$, the shock settles down at larger radii as $\Phi_{13}$ is increased. The indefinite increase of radial magnetic flux is not possible, as there exists a cutoff value of $\Phi_{13}$ for which shock conditions are not satisfied. Furthermore, we calculate $R$ and $S$ as in Figures 4(b)–(c) and observe that both quantities are decreased when $\Phi_{13}$ is increased.

In Figure 5, we depict the comparison of shock properties as a function of the isorotation parameter ($F_{15}$). In panels (a)–(c) of Figure 5, we plot $r_{\rm sh}$, $R$, and $\Psi$ for different values of $\mathcal{L}$. Here, we choose the model parameters as $\mathcal{E} = 1.0015$, $\Phi_{13} = 5.0$, and $a_{\rm k} = 0.99$. The solid, dotted, and dashed curves denote the results for $\mathcal{L} = 1.925$, $1.950$, and $1.975$, respectively. On the contrary, in Figures 5(d)–(f), we present the results of $r_{\rm sh}$, $R$, and $\Psi$ for different $\mathcal{E}$, where the solid, dotted, and dashed curves are for $\mathcal{E} = 1.0005$, $1.0015$, and $1.0025$, respectively. The model parameters are chosen as $\mathcal{L} = 1.95$, $\Phi_{13} = 5.0$, and $a_{\rm k} = 0.99$. In both scenarios, we notice that the shock location remains nearly unaffected due to the increase in $F_{15}$. Consequently, both the compression ratio ($R$) and shock strength ($\Psi$) exhibit negligible variation with $F_{15}$ as well. Because of this, from now onward, we refrain from examining the influence of $F_{15}$ on the shock properties, unless stated otherwise.

As previously noted, shock-induced global GRMHD solutions are favored over shock-free solutions due to their elevated entropy content. However, the role of the magnetic fields in contributing to the flow entropy is not well understood. To
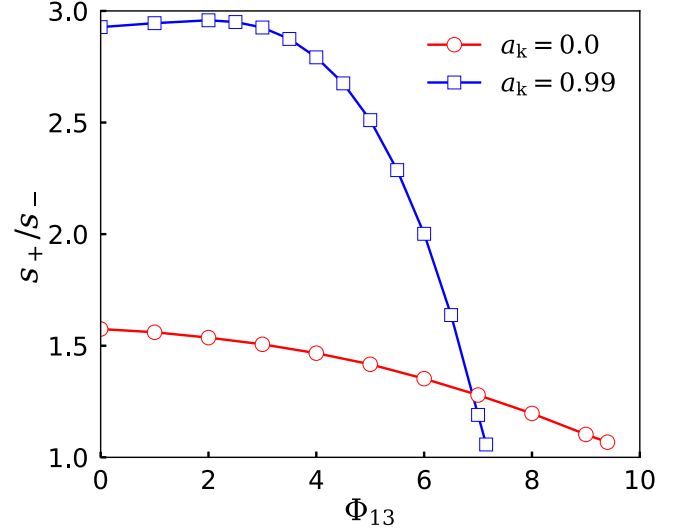


**Figure 6.** Plot of ratio of postshock ($s_+$) to preshock ($s_-$) entropy functions across the shock front with $\Phi_{13}$. The open circles and open squares joined with solid lines denote the results obtained for nonrotating ($a_{\rm k} = 0.0$) and rapidly rotating ($a_{\rm k} = 0.99$) BHs. Here, we choose $\mathcal{L} = 3.15$ for $a_{\rm k} = 0.0$ and $\mathcal{L} = 1.95$ for $a_{\rm k} = 0.99$, while the other model parameters are kept fixed, as $\mathcal{E} = 1.001$ and $F_{15} = 7.5$. See the text for details.

address this, we calculate the ratio of entropy functions measured immediately after ($s_+$) and before ($s_-$) the shock transition. The obtained results are depicted in Figure 6, where we plot the variation of $s_+/s_-$ with $\Phi_{13}$ for flows with fixed energy $\mathcal{E} = 1.001$ and isorotation parameter $F_{15} = 7.5$. In the figure, the open circles joined with solid lines represent the results corresponding to the shocked accretion solutions around a nonrotating BH with $a_{\rm k} = 0.0$ and $\mathcal{L} = 3.15$. Similarly, the open squares joined with solid lines are for a rapidly rotating BH with $a_{\rm k} = 0.99$, and $\mathcal{L} = 1.95$. We observe that for a chosen set of model parameters, $s_+/s_-$ is maximum for $\Phi_{13} = 0.0$, irrespective of $a_{\rm k}$ values, and it generally decreases with the increase of $\Phi_{13}$. When $\Phi_{13}$ reaches a critical limit, the ratio $s_+/s_-$ approaches unity, indicating that the shock ceases to exist, as the shock conditions are not favorable. Indeed, it is worth noting that this critical limit of $\Phi_{13}$ is not universal, as it varies depending on the other model parameters.

### 4.4. Parameter Space for Standing Shock

It has already been indicated that shock-induced GRMHD accretion solutions are not isolated solutions; instead, these solutions continue to exist for a wide range of model parameters—namely, $\mathcal{E}$, $\mathcal{L}$, $\Phi_{13}$, $F_{15}$, and $a_{\rm k}$. Hence, it is useful to identify the ranges of model parameters that admit shocked accretion solutions. Toward this, in Figure 7, we separate the effective domain of the parameter space in the $\mathcal{L}$–$\mathcal{E}$ plane and examine the modification of the parameter space for different $\Phi_{13}$, where the spin of the BH and $F_{15}$ are kept fixed as $a_{\rm k} = 0.99$ and $5.0$. The regions enclosed by the solid (black), dotted (red), and dashed (blue) curves are for $\Phi_{13} = 5.0$, $7.5$, and $10.0$, respectively. We observe that the parameter space shifts toward the lower-angular-momentum ($\mathcal{L}$) domain as $\Phi_{13}$ is increased. This happens because the increase of $\Phi_{13}$ effectively enhances the angular momentum transport outward (Mitra et al. 2022), leading to the reduction of $\mathcal{L}$, which allows the shock transition for higher $\Phi_{13}$. Similarly, in Figure 8, we present the modification of the parameter space for different $a_{\rm k}$.
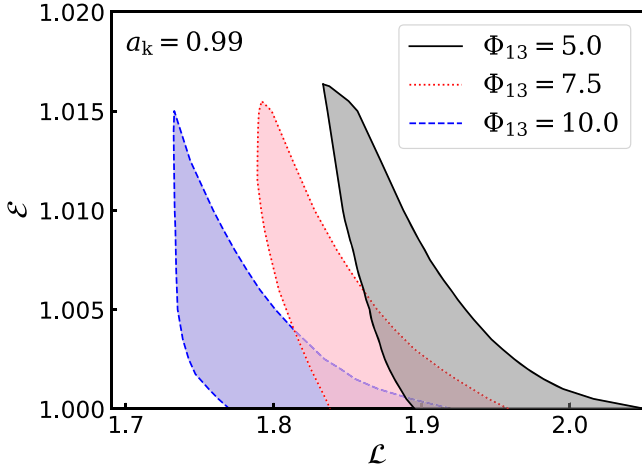
**Figure 7.** Plot of shock parameter space in the $\mathcal{L}$–$\mathcal{E}$ plane for different radial magnetic fluxes ($\Phi_{13}$) around a rotating BH. Here, we choose $a_k = 0.99$ and $F_{15} = 5.0$. The effective areas bounded by the solid (black), dotted (red), and dashed (blue) curves correspond to $\Phi_{13} = 5.0$, 7.5, and 10.0, respectively. See the main text for details.
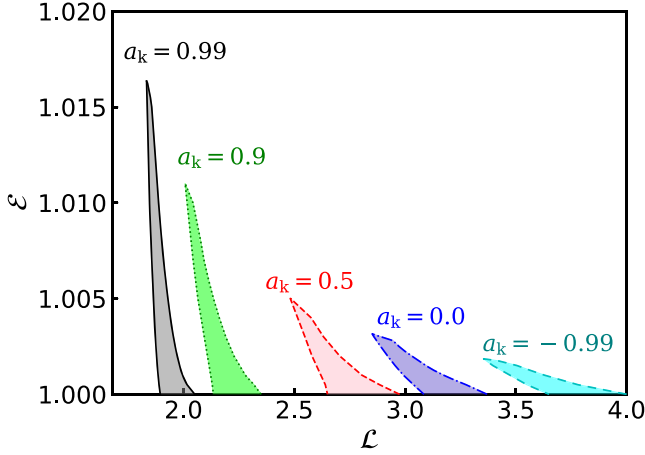


**Figure 8.** Modification of shock parameter space in the $\mathcal{L}$–$\mathcal{E}$ plane with the BH spin varied as $a_k = 0.99$, 0.9, 0.5, 0.0, and $-0.99$ (from left to right). Here, we fix $\Phi_{13} = 5.0$ and $F_{15} = 5.0$. See the main text for details.

Here, we choose $\Phi_{13} = 5.0$ and $F_{15} = 5.0$. We observe that the effective regions bounded by the different line styles are obtained for $a_k = 0.99$, 0.9, 0.5, 0.0, and $-0.99$ (from left to right). We again observe that the parameter space is shifted to the lower-angular-momentum side as the BH spin is increased (Aktar et al. 2015; Dihingia et al. 2019). This is not surprising, because a relatively low-angular-momentum flow experiences a shock transition around a BH of higher $a_k$ (Das & Chakrabarti 2008). Overall, we stress that both $a_k$ and $\Phi_{13}$ play a pivotal role in determining the shock parameter space of the GRMHD flow.

Subsequently, we investigate the critical radial magnetic flux ($\Phi_{13}^{\mathrm{cri}}$) necessary to render global GRMHD accretion solutions around BHs harboring shocks. In doing so, we calculate $\Phi_{13}^{\mathrm{cri}}$ for various values of BH spin ($a_k$), while keeping the isorotation parameter and accretion rate fixed at $F_{15} = 5.0$ and $\dot{m} = 0.001$, respectively, with the energy ($\mathcal{E}$) and angular momentum ($\mathcal{L}$) of the flow allowed to vary freely. The obtained results are depicted in Figure 9, where the open circles connected by solid lines represent the variation of $\Phi_{13}^{\mathrm{cri}}$ with $a_k$. We observe that shock-induced GRMHD accretion solutions exist for a wide
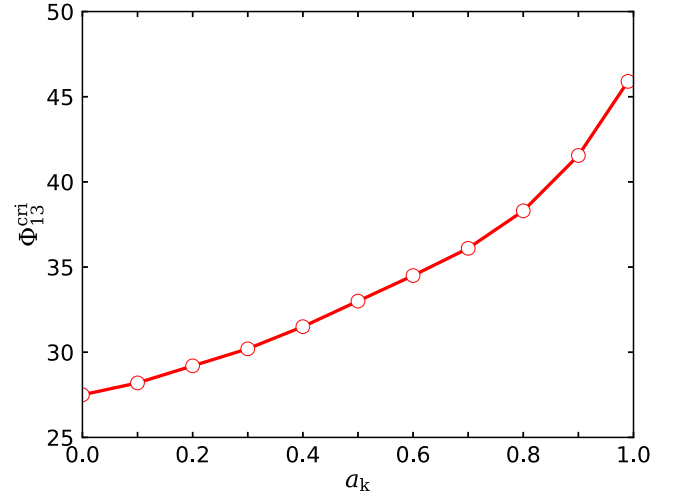


**Figure 9.** Variation of maximum radial magnetic flux ($\Phi_{13}^{\mathrm{max}}$) as a function of BH spin ($a_k$) for shocked accretion solutions. Here, we choose $F_{15} = 5.0$, and ($\mathcal{E}$, $\mathcal{L}$) are chosen freely. See the main text for details.

range of $\Phi_{13}$. In particular, we find that for $a_k = 0.0$, $\Phi_{13}^{\mathrm{cri}} = 27.5$, and $\Phi_{13}^{\mathrm{cri}}$ increases with the increase of $a_k$, where $\Phi_{13}^{\mathrm{cri}} = 45.9$ for $a_k = 0.99$. This finding evidently indicates that GRMHD accretion flows with stronger magnetic fields continue to sustain shocks around rapidly rotating BHs and vice versa. What is more, by analyzing the disk magnetic flux, one can speculate whether the magnetized accretion flow is consistent with the results of either a MAD or the standard and normal evolution state (Narayan et al. 2012; Chatterjee & Narayan 2022). To assess this, we calculate the upper limit of the magnetic flux entering the ergosphere as $\int_0^{2\pi} -\sqrt{-g} \, {}^*F^{rt}d\phi = 3.23 \times 10^{18}\Phi_{13}^{\mathrm{cri}} \, \mathrm{G \, cm}^2$, and find that the GRMHD accretion flows under consideration remain significantly below the MAD limit, $\sim 10^{21} \, \mathrm{G \, cm}^2$, as indicated by Sádowski (2016), for a BH with a mass of $10 M_\odot$ and a spin parameter within the range $0 \leqslant a_k < 0.99$.

## 5. Conclusions

In this work, we study the global structure of the shock-induced, magnetized, advective accretion flow around rotating BHs. In doing this, we solve the GRMHD equations that govern the flow motion in the steady state and obtain comprehensive solutions for the global transmagnetosonic accretion flow around weakly ($a_k \rightarrow 0$) as well as rapidly ($a_k = 0.99$) rotating BHs. We observe that depending on the model parameters—namely $\mathcal{E}$, $\mathcal{L}$, $\Phi_{13}$, $F_{15}$, and $a_k$—the GRMHD flow often possesses MCPs ($r_{\mathrm{in}}$ and $r_{\mathrm{out}}$). It is noteworthy that the accretion solutions simultaneously passing through both $r_{\mathrm{in}}$ and $r_{\mathrm{out}}$ are of special importance, as they may harbor shock waves, and shock-induced accretion solutions are potentially promising in explaining the spectrotemporal properties of BH sources (Chakrabarti & Titarchuk 1995; Nandi et al. 2012; Das et al. 2021). With this, we summarize our present findings below.

1. We obtain shock-induced global GRMHD accretion solutions around rotating BHs for the first time, to the best of our knowledge. We observe that irrespective of the BH spin ($a_k$), the shock forms farther out as the radial magnetic flux ($\Phi_{13}$) is increased for flows with fixed model parameters ($\mathcal{E}$, $\mathcal{L}$, and $F_{15}$). We further notice that

the entropy of the shocked accretion solution always remains higher than the shock-free solution, confirming that shocked solutions are thermodynamically preferred (see Figure 1).

2. We observe that magnetic fields play an important role in regulating the structure of the shocked GRMHD accretion flow around BHs (see Figures 2–3). In general, the accretion flow largely remains gas-pressure-dominated ($\beta > 10$) throughout the disk, except at the inner part of the disk ($r < 10 r_g$). Moreover, we find that in the preshock regime, the toroidal field follows a self-similar radial profile as $b^\phi \propto r^{-5/4}$ (Yuan & Narayan 2014), but it becomes steeper in the postshock flow, in order to maintain the continuity of the radial flux balance across the shock front (see Section 3). The toridal field becomes more intense around the rotating BHs, due to the effect of frame-dragging, and for a $10 M_\odot$ BH of spin $a_k = 0.99$, it becomes very strong, as $b^\phi \sim 10^{7-9}$ G, near the horizon. On the contrary, we find $b^\phi \sim 10^{5-6}$ G in the region close to the horizon of a nonrotating ($a_k = 0.0$) BH.

3. We also examine the best-fit power-law profiles of density ($\rho$) and temperature ($T$) in both the pre- and postshock regimes around weakly rotating ($a_k \to 0.0$) as well as rapidly rotating ($a_k = 0.99$) BHs. We ascertain that in the preshock regime, the density and temperature profiles of the GRMHD flow remain unaffected due to BH spin and are obtained as $\rho \propto r^{-3/2}$ and $T \propto r^{-3/4}$, respectively. These findings are in agreement with the results of Narayan & Yi (1994) and Yuan & Narayan (2014). However, due to shock compression, both $\rho$ and $T$ follow steeper power-law profiles, as $\rho \propto r^{-2}$ and $T \propto r^{-1}$ for $a_k = 0.99$ and as $\rho \propto r^{-1.75}$ and $T \propto r^{-0.8}$ for $a_k = 0.00$ (see Figures 2–3).

4. A convergent GRMHD shocked accretion flow yields a hot and dense postshock flow (see Figures 2–3) resembling a PSC, containing hot electrons. When soft photons from the preshock flow interact with the PSC, they undergo inverse Comptonization, producing hard-X-ray radiation, commonly observed from BH X-ray binaries (Chakrabarti & Titarchuk 1995; Nandi et al. 2012, 2018; Iyer et al. 2015). Since the PSC characteristics (i.e., its size, density, and temperature) are determined by the shock properties, and the magnetic fields ($\Phi_{13}$ and $F_{15}$) control $r_{sh}$, $R$, and $\Psi$ (see Figures 4–5), it is therefore evident that magnetic fields play a crucial role in determining the spectral properties of BHs.

5. Moreover, we find that the shock-induced GRMHD accretion solutions are not isolated solutions, as solutions of these kinds continue to exist for a wide range of model parameters—namely $\mathcal{E}$, $\mathcal{L}$, $\Phi_{13}$, $F_{15}$, and $a_k$. To ascertain this, we separate the parameter space in the $\mathcal{L}$–$\mathcal{E}$ plane for different $\Phi_{13}$, which admits GRMHD shock solutions around rapidly rotating ($a_k = 0.99$) BHs (see Figure 7). Moreover, we examine the modification of the shock parameter space (in the $\mathcal{L}$–$\mathcal{E}$ plane) for various BH spin ($a_k$) values and observe that GRMHD accretion flows exhibit shocks within the spin range $-0.99 < a_k < 0.99$ (see Figure 8).

6. We calculate the critical radial magnetic flux ($\Phi_{13}^{cri}$), representing the threshold beyond which shocks cease to exist in the GRMHD accretion flow around BHs. We

observe a strong dependence of $\Phi_{13}^{cri}$ on the spin of the BH ($a_k$), with $\Phi_{13}^{cri}$ being higher for $a_k = 0.99$ compared to $a_k = 0.0$ (see Figure 9). We also observe that the shock-induced GRMHD accretion flow under consideration remains restricted below the MAD threshold.

Finally, we indicate the limitations of the present work, as it is carried out based on assumptions. We neglect the polar component of the magnetic fields ($b^\theta$), considering the fact that the disk is confined around the equatorial plane. Indeed, $b^\theta$ is expected to play a crucial role in launching jets and outflows (Fendt 2006; McKinney 2006; Dihingia et al. 2021, and references therein). We ignore the effect of radiative cooling, although its presence is relevant. Moreover, we consider a single-temperature fluid, neglecting two-temperature descriptions of ions and electrons. We also work by adopting the ideal MHD limit, ignoring the resistive MHD approach. Indeed, the implementation of these complexities exceeds the scope of the present paper, and we plan to take them up in future endeavors.

### Data Availability

The data underlying this article will be made available with reasonable request.

### Appendix A
### Derivation of Wind Equations

The radial momentum equation, angular momentum equation, and energy equation are obtained as

$$R_0 + R_v \frac{dv}{dr} + R_\Theta \frac{d\Theta}{dr} + R_\lambda \frac{d\lambda}{dr} = 0, \tag{A1}$$

$$\mathcal{L}_0 + \mathcal{L}_v \frac{dv}{dr} + \mathcal{L}_\Theta \frac{d\Theta}{dr} + \mathcal{L}_\lambda \frac{d\lambda}{dr} = 0, \tag{A2}$$

$$\mathcal{E}_0 + \mathcal{E}_v \frac{dv}{dr} + \mathcal{E}_\Theta \frac{d\Theta}{dr} + \mathcal{E}_\lambda \frac{d\lambda}{dr} = 0, \tag{A3}$$

and the coefficients in Equations (A1)–(A3) are given below. In order to express these coefficients, we begin with the derivative of the four-velocities $u'_\mu = \frac{du^\mu}{dr}$, where all the Greek symbols correspond to the following coordinates $\mu \equiv (t, r, \theta, \phi)$:

$$u'_\mu = u_{\mu_0} + u_{\mu_v} v' + u_{\mu_\lambda} \lambda', \quad u^{\mu'} = u_0^\mu + u_v^\mu v' + u_\lambda^\mu \lambda',$$

$$u_0^\mu = \frac{\partial u^\mu}{\partial r}, \quad u_v^\mu = \frac{\partial u^\mu}{\partial v}, \quad u_\lambda^\mu = \frac{\partial u^\mu}{\partial \lambda},$$

$$u_{\mu_0} = \frac{\partial u_\mu}{\partial r}, \quad u_{\mu_v} = \frac{\partial u_\mu}{\partial v}, \quad u_{\mu_\lambda} = \frac{\partial u_\mu}{\partial \lambda}.$$

With the following definitions of $b^r$, $b^\phi$ (see Equation (12)), and $b^t$,

$$b^r = -\frac{\gamma_\phi^2(\Phi + F\lambda)}{u^t r^2 (v^2 - 1)}, \quad b^\phi = \frac{Fv^2 - \gamma_\phi^2(F + \Phi\Omega)}{u^r r^2 (v^2 - 1)},$$

$$b^t = -\frac{u_r}{u_t}b^r + \lambda b^\phi,$$

we can write,

$$b^{\mu\prime} = b_0^\mu + b_v^\mu v' + b_\lambda^\mu \lambda', \text{ where } b_0^\mu = \frac{\partial b^\mu}{\partial r}, b_v^\mu = \frac{\partial b^\mu}{\partial v},$$

$$b_\lambda^\mu = \frac{\partial b^\mu}{\partial \lambda}.$$

In this way, the derivative of the square of the magnetic field $\mathcal{B} = b_\mu b^\mu$ is expressed as

$$\mathcal{B}' = \mathcal{B}_0 + \mathcal{B}_v v' + \mathcal{B}_\lambda \lambda', \ \mathcal{B}_0 = \frac{\partial \mathcal{B}}{\partial r}, \mathcal{B}_v = \frac{\partial \mathcal{B}}{\partial v}, \mathcal{B}_\lambda = \frac{\partial \mathcal{B}}{\partial \lambda}.$$

Similarly,

$$h'_{\text{tot}} = h_t^0 + h_t^v v' + h_t^\Theta \Theta' + h_t^\lambda \lambda', h_t^0 = \frac{\partial h_{\text{tot}}}{\partial r},$$

$$h_t^v = \frac{\partial h_{\text{tot}}}{\partial v}, h_t^\Theta = \frac{\partial h_{\text{tot}}}{\partial \Theta}, h_t^\lambda = \frac{\partial h_{\text{tot}}}{\partial \lambda},$$

and

$$\mathcal{F}' = \frac{d\mathcal{F}}{dr} = \mathcal{F}_1 + \mathcal{F}_2 \frac{d\lambda}{dr}, \mathcal{F}_1 = \frac{\partial \mathcal{F}}{\partial r}, \mathcal{F}_2 = \frac{\partial \mathcal{F}}{\partial \lambda}, \Delta' = \frac{d\Delta}{dr}.$$

With these definitions, we express the coefficients of the Equations (A1)–(A3) as follows:

$$R_0 = (R_a + \mathcal{A}R_1)/\rho h_{\text{tot}}, \ \mathcal{A} = (g^{rr} + u^r u^r),$$

$$R_1 = \frac{\mathcal{B}_0}{2} - \frac{3\Theta\rho}{r\tau} + \frac{\mathcal{F}_1\Theta\rho}{\tau\mathcal{F}} - \frac{\Theta\rho\Delta'}{\tau\Delta},$$

$$R_a = -b^r b_0^r (2 + g_{rr}u^r u^r) + h_{\text{tot}}u^r u_0^r \rho$$
$$- b^r u^r (u_t b_0^t + u_\phi b_0^\phi) + R_b, \ R_b$$
$$= -g^{rr} b^{r^2}\left(1 - \frac{1}{2}g_{rr}u^{r^2}\right)g'_{rr} + R_c,$$

$$R_c = \frac{\rho h_{\text{tot}}}{2}g^{rr}u^{r^2}g_{rr}' + \frac{g^{rr}b^{t^2}}{2}g'_{tt} + g^{rr}g'_{t\phi}b^t b^\phi + \frac{g^{rr}}{2}b^{\phi^2}g'_{\phi\phi}$$
$$- \frac{g^{\theta\theta}}{2}b^{r^2}g_{\theta\theta}' - \mathcal{S}_1(b^{r^2} + 2b^r u^r b^t u_t) + R_d,$$

$$R_d = -2b^r u^r b^t u_\phi \mathcal{S}_2 - 2b^r u^r b^\phi u_t \mathcal{S}_2 - \mathcal{S}_3 g_{rr}u^{r^2}b^t + \mathcal{S}_4 h_{\text{tot}}u^t \rho$$
$$- g_{rr}u^{r^2}b^\phi \mathcal{S}_5 + h_{\text{tot}}\rho u^\phi \mathcal{S}_6 - \mathcal{S}_7(b^{r^2} + 2b^r u^r b^\phi u_\phi),$$

$$\mathcal{S}_1 = \frac{1}{2}(g^{tt}g'_{tt} + g^{t\phi}g'_{t\phi}), \mathcal{S}_2 = \frac{1}{2}(g^{tt}g'_{t\phi} + g^{t\phi}g'_{\phi\phi}),$$

$$\mathcal{S}_3 = -\frac{g^{rr}}{2}(b^t g'_{tt} + b^\phi g'_{t\phi}), \mathcal{S}_4 = -\frac{g^{rr}}{2}(u^t g'_{tt} + u^\phi g'_{t\phi}),$$

$$\mathcal{S}_5 = -\frac{g^{rr}}{2}(b^t g'_{t\phi} + b^\phi g'_{\phi\phi}), \mathcal{S}_6 = -\frac{g^{rr}}{2}$$

$$\times (u^t g'_{t\phi} + u^\phi g'_{\phi\phi}), \mathcal{S}_7 = \frac{1}{2}(g^{t\phi}g'_{t\phi} + g^{\phi\phi}g'_{\phi\phi}).$$

$$R_v = (R_e + \mathcal{A}R_2)/\rho h_{\text{tot}}, R_2 = \frac{\mathcal{B}_v}{2} - \frac{2\Theta\rho(1 + v^2\gamma_v^2)}{\tau\mathcal{F}},$$

$$R_e = -b^r b_v^r(2 + g_{rr}u^r u^r) + h_{\text{tot}}u^r u_v^r \rho - b^r u^r(u_t b_v^t + u_\phi b_v^\phi),$$

$$R_\Theta = \frac{1}{\tau h_{\text{tot}}}, R_\lambda = (R_f + \mathcal{A}R_3)/\rho h_{\text{tot}}, R_3 = \frac{\mathcal{B}_\lambda}{2} + \frac{\mathcal{F}_2\Theta\rho}{\tau\mathcal{F}},$$

$$R_f = -b^r b_\lambda^r(2 + g_{rr}u^r u^r) - b^r u^r(u_t b_\lambda^t + u_\phi b_\lambda^\phi).$$

$$\mathcal{L}_0 = h_t^0 u_\phi + h_{\text{tot}}u_{\phi_0}$$
$$- \frac{g_{t\phi}b^r b_0^t + b_0^r b_\phi + g_{\phi\phi}b^r b_0^\phi - b^r b^t g'_{t\phi} + b^r b^\phi g'_{\phi\phi}}{u^r \rho}$$
$$- \frac{3b^r b_\phi}{2ru^r\rho} + \frac{\mathcal{F}_1 b^r b_\phi}{2\mathcal{F}u^r\rho} - \frac{b^r b_\phi \Delta'}{2u^r\Delta\rho} + \frac{b^r u_0^r b_\phi}{u^{r^2}\rho},$$

$$\mathcal{L}_v = h_t^v u_\phi + h_{\text{tot}}u_{\phi_v} - \frac{g_{t\phi}b^r b_v^t + b_v^r b_\phi + g_{\phi\phi}b^r b_v^\phi}{u^r\rho}$$
$$+ \frac{b^r u_v^r b_\phi}{u^{r^2}\rho} - \frac{b^r(1 + v^2\gamma_v^2)b_\phi}{u^r v\rho},$$

$$\mathcal{L}_\Theta = h_t^\Theta u_\phi$$
$$- \frac{b^r b_\phi}{2u^r\Theta\rho}, \mathcal{L}_\lambda = h_t^\lambda u_\phi + h_{\text{tot}}u_{\phi_\lambda}$$
$$- \frac{g_{t\phi}b^r b_\lambda^t}{u^r\rho} + \frac{\mathcal{F}_2 b^r b_\phi}{2\mathcal{F}u^r\rho} - \frac{b_\lambda^r b_\phi}{u^r\rho} - \frac{g_{\phi\phi}b^r b_\lambda^\phi}{u^r\rho}.$$

$$\mathcal{E}_0 = -h_t^0 u_t - h_{\text{tot}}u_{t_0}$$
$$+ \frac{g_{tt}b^r b_0^t + b_0^r b_t + g_{t\phi}b^r b_0^\phi - b^r b^\phi g'_{t\phi} + b^r b^t g'_{tt}}{u^r\rho}$$
$$+ \frac{3b^r b_t}{2ru^r\rho} - \frac{\mathcal{F}_1 b^r b_t}{2\mathcal{F}u^r\rho} - \frac{b^r b_t\Delta'}{2u^r\Delta\rho} - \frac{b^r u_0^r b_t}{u^{r^2}\rho},$$

$$\mathcal{E}_v = -h_t^v u_t - h_{\text{tot}}u_{t_v} + \frac{g_{tt}b^r b_v^t + b_v^r b_t + g_{t\phi}b^r b_v^\phi}{u^r\rho}$$
$$- \frac{b^r u_v^r b_t}{u^{r^2}\rho} + \frac{b^r(1 + v^2\gamma_v^2)b_t}{u^r v\rho},$$

$$\mathcal{E}_\Theta = -h_t^\Theta u_t$$
$$+ \frac{b^r b_t}{2u^r\Theta\rho}, \mathcal{E}_\lambda = -h_t^\lambda u_t - h_{\text{tot}}u_{t_\lambda}$$
$$+ \frac{g_{tt}b^r b_\lambda^t}{u^r\rho} - \frac{\mathcal{F}_2 b^r b_t}{2\mathcal{F}u^r\rho} + \frac{b_\lambda^r b_t}{u^r\rho} + \frac{g_{t\phi}b^r b_\lambda^\phi}{u^r\rho}.$$

## Appendix B
## Expressions of Numerator and Denominator

As mentioned previously, we express the wind Equation (18) as

$$\frac{dv}{dr} = \frac{\mathcal{N}(r, a_k, v, \Theta, \lambda, \Phi, F)}{\mathcal{D}(r, a_k, v, \Theta, \lambda, \Phi, F)}. \tag{B1}$$

Here, the numerator ($\mathcal{N}$) is given by

$$\mathcal{N} = -R_0 - R_\Theta\Theta_{11} - R_\lambda\lambda_{11}, \tag{B2}$$

and the denominator $(\mathcal{D})$ is given by

$$\mathcal{D} = R_v + R_\Theta \Theta_{12} + R_\lambda \lambda_{12}, \quad (B3)$$

where

$$\Theta_{11} = \frac{\mathcal{E}_\lambda \mathcal{L}_0 - \mathcal{E}_0 \mathcal{L}_\lambda}{-\mathcal{E}_\lambda \mathcal{L}_\Theta + \mathcal{E}_\Theta \mathcal{L}_\lambda}, \quad \Theta_{12} = \frac{\mathcal{E}_\lambda \mathcal{L}_v - \mathcal{E}_v \mathcal{L}_\lambda}{-\mathcal{E}_\lambda \mathcal{L}_\Theta + \mathcal{E}_\Theta \mathcal{L}_\lambda},$$

$$\lambda_{11} = \frac{-\mathcal{E}_\Theta \mathcal{L}_0 + \mathcal{E}_0 \mathcal{L}_\Theta}{-\mathcal{E}_\lambda \mathcal{L}_\Theta + \mathcal{E}_\Theta \mathcal{L}_\lambda}, \quad \lambda_{12} = \frac{-\mathcal{E}_\Theta \mathcal{L}_v + \mathcal{E}_v \mathcal{L}_\Theta}{-\mathcal{E}_\lambda \mathcal{L}_\Theta + \mathcal{E}_\Theta \mathcal{L}_\lambda}.$$

## ORCID iDs

Samik Mitra ⬤ https://orcid.org/0000-0002-5730-0376
Santabrata Das ⬤ https://orcid.org/0000-0003-4399-5047

## References

Abramowicz, M. A., & Fragile, P. C. 2013, LRR, 16, 1
Aktar, R., Das, S., & Nandi, A. 2015, MNRAS, 453, 3414
Aktar, R., Das, S., Nandi, A., & Sreehari, H. 2017, MNRAS, 471, 4806
Anile, A. M. 1990, Relativistic Fluids and Magneto-fluids (Cambridge: Cambridge Univ. Press)
Appl, S., & Camenzind, M. 1988, A&A, 206, 258
Avara, M. J., McKinney, J. C., & Reynolds, C. S. 2016, MNRAS, 462, 636
Balbus, S. A., & Hawley, J. F. 1991, ApJ, 376, 214
Balbus, S. A., & Hawley, J. F. 1998, RvMP, 70, 1
Becker, P. A., Das, S., & Le, T. 2008, ApJL, 677, L93
Becker, P. A., & Kazanas, D. 2001, ApJ, 546, 429
Begelman, M. C., & Pringle, J. E. 2007, MNRAS, 375, 1070
Bisnovatyi-Kogan, G. S., & Lovelace, R. V. E. 2011, arXiv:1104.4866
Bisnovatyi-Kogan, G. S., & Ruzmaikin, A. A. 1974, Ap&SS, 28, 45
Bisnovatyi-Kogan, G. S., & Ruzmaikin, A. A. 1976, Ap&SS, 42, 401
Chakrabarti, S., & Titarchuk, L. G. 1995, ApJ, 455, 623
Chakrabarti, S. K. 1989, ApJ, 347, 365
Chakrabarti, S. K., & Das, S. 2004, MNRAS, 349, 649
Chatterjee, K., Chael, A., Tiede, P., et al. 2023, Galax, 11, 38
Chatterjee, K., & Narayan, R. 2022, ApJ, 941, 30
Chattopadhyay, I., & Ryu, D. 2009, ApJ, 694, 492
Das, S. 2007, MNRAS, 376, 1659
Das, S., Becker, P. A., & Le, T. 2009, ApJ, 702, 649
Das, S., & Chakrabarti, S. K. 2004, IJMPD, 13, 1955
Das, S., & Chakrabarti, S. K. 2007, MNRAS, 374, 729
Das, S., & Chakrabarti, S. K. 2008, MNRAS, 389, 371
Das, S., Chattopadhyay, I., & Chakrabarti, S. K. 2001, ApJ, 557, 983
Das, S., Chattopadhyay, I., Nandi, A., & Molteni, D. 2014, MNRAS, 442, 251
Das, S., Nandi, A., Agrawal, V. K., Dihingia, I. K., & Majumder, S. 2021, MNRAS, 507, 2777
Das, S., Nandi, A., Stalin, C. S., et al. 2022, MNRAS, 514, 1940
Das, S., & Sarkar, B. 2018, MNRAS, 480, 3446
De Villiers, J.-P., Hawley, J. F., & Krolik, J. H. 2003, ApJ, 599, 1238
Dihingia, I. K., Das, S., Maity, D., & Chakrabarti, S. 2018, PhRvD, 98, 083004
Dihingia, I. K., Das, S., Maity, D., & Nandi, A. 2019, MNRAS, 488, 2412
Dihingia, I. K., Das, S., Prabhakar, G., & Mandal, S. 2020, MNRAS, 496, 3043
Dihingia, I. K., Vaidya, B., & Fendt, C. 2021, MNRAS, 505, 3596
Event Horizon Telescope Collaboration, Akiyama, K., Algaba, J. C., et al. 2021, ApJL, 910, L13
Fendt, C. 2006, ApJ, 651, 272
Frank, J., King, A., & Raine, D. J. 2002, Accretion Power in Astrophysics: Third Edition (Cambridge: Cambridge Univ. Press)
Fukue, J. 1987, PASJ, 39, 309
Fukumura, K., Hendry, D., Clark, P., Tombesi, F., & Takahashi, M. 2016, ApJ, 827, 31
Fukumura, K., & Kazanas, D. 2007, ApJ, 669, 85
Fukumura, K., Takahashi, M., & Tsuruta, S. 2007, ApJ, 657, 415
Fukumura, K., & Tsuruta, S. 2004, ApJ, 611, 964
Gammie, C. F., McKinney, J. C., & Tóth, G. 2003, ApJ, 589, 444

Hawley, J. F. 2001, ApJ, 554, 534
Hirose, S., Krolik, J. H., De Villiers, J.-P., & Hawley, J. F. 2004, ApJ, 606, 1083
Igumenshchev, I. V., Narayan, R., & Abramowicz, M. A. 2003, ApJ, 592, 1042
Iyer, N., Nandi, A., & Mandal, S. 2015, ApJ, 807, 108
Jacquemin-Ide, J., Rincon, F., Tchekhovskoy, A., & Liska, M. 2024, MNRAS, 532, 1522
Kato, Y., Mineshige, S., & Shibata, K. 2004, ApJ, 605, 307
Kerr, R. P. 1963, PhRvL, 11, 237
Kim, J., Garain, S. K., Chakrabarti, S. K., & Balsara, D. S. 2019, MNRAS, 482, 3636
Kumar, R., Singh, C. B., Chattopadhyay, I., & Chakrabarti, S. K. 2013, MNRAS, 436, 2864
Lichnerowicz, A. 1970, PhyS, 2, 221
Liska, M. T. P., Musoke, G., Tchekhovskoy, A., Porth, O., & Beloborodov, A. M. 2022, ApJL, 935, L1
Lu, J. F. 1985, A&A, 148, 176
Lu, J.-F., Gu, W.-M., & Yuan, F. 1999, ApJ, 523, 340
Majumder, S., Sreehari, H., Aftab, N., et al. 2022, MNRAS, 512, 2508
Mandal, S., & Chakrabarti, S. K. 2005, A&A, 434, 839
Manikantan, V., Kaaz, N., Jacquemin-Ide, J., et al. 2024, ApJ, 965, 175
McKinney, J. C. 2006, MNRAS, 368, 1561
McKinney, J. C., & Gammie, C. F. 2004, ApJ, 611, 977
Mishra, B., Begelman, M. C., Armitage, P. J., & Simon, J. B. 2020, MNRAS, 492, 1855
Mishra, B., Fragile, P. C., Johnson, L. C., & Kluźniak, W. 2016, MNRAS, 463, 3437
Mitra, S., Ghoreyshi, S. M., Mosallanezhad, A., Abbassi, S., & Das, S. 2023, MNRAS, 523, 4431
Mitra, S., Maity, D., Dihingia, I. K., & Das, S. 2022, MNRAS, 516, 5092
Nandi, A., Das, S., Majumder, S., et al. 2024, MNRAS, 531, 1149
Nandi, A., Debnath, D., Mandal, S., & Chakrabarti, S. K. 2012, A&A, 542, A56
Nandi, A., Mandal, S., Sreehari, H., et al. 2018, Ap&SS, 363, 90
Narayan, R., Igumenshchev, I. V., & Abramowicz, M. A. 2003, PASJ, 55, L69
Narayan, R., & Yi, I. 1994, ApJL, 428, L13
Narayan, R., & Yi, I. 1995, ApJ, 444, 231
Narayan, R. S. Å., Dowski, A., Penna, R. F., & Kulkarni, A. K. 2012, MNRAS, 426, 3241
Oda, H., Machida, M., Nakamura, K. E., & Matsumoto, R. 2007, PASJ, 59, 457
Oda, H., Machida, M., Nakamura, K. E., & Matsumoto, R. 2010, ApJ, 712, 639
Oda, H., Machida, M., Nakamura, K. E., Matsumoto, R., & Narayan, R. 2012, PASJ, 64, 15
Olivares, S., Moscibrodzka, H. R., & Porth, O., M. A. 2023, A&A, 678, A141
Peitz, J., & Appl, S. 1997, MNRAS, 286, 681
Porth, O., Chatterjee, K., Narayan, R., et al. 2019, ApJS, 243, 26
Porth, O., Olivares, H., Mizuno, Y., et al. 2017, ComAC, 4, 1
Poutanen, J. 1998, in Theory of Black Hole Accretion Disks, ed. M. A. Abramowicz, G. Björnsson, & J. E. Pringle (Cambridge: Cambridge Univ. Press), 100
Riffert, H., & Herold, H. 1995, ApJ, 450, 508
Ryu, D., Chakrabarti, S. K., & Molteni, D. 1997, ApJ, 474, 378
Sądowski, A. 2016, MNRAS, 459, 4397
Sarkar, B., & Das, S. 2015, in ASI Conf. Ser. 12, Recent Trends in the Study of Compact Objects (RETCO-II): Theory and Observation, ed. I. Chattopadhyay et al. (Hyderabad: ASI), 91
Sarkar, B., & Das, S. 2016, MNRAS, 461, 190
Sarkar, B., Das, S., & Mandal, S. 2018, MNRAS, 473, 2415
Sen, G., Maity, D., & Das, S. 2022, JCAP, 2022, 048
Shafee, R., McKinney, J. C., Narayan, R., et al. 2008, ApJL, 687, L25
Shakura, N. I., & Sunyaev, R. A. 1973, A&A, 24, 337
Suková, P., Charzyński, S., & Janiuk, A. 2017, MNRAS, 472, 4327
Suková, P., & Janiuk, A. 2015, MNRAS, 447, 1565
Takahashi, M., Goto, J., Fukumura, K., Rilett, D., & Tsuruta, S. 2006, ApJ, 645, 1408
Takahashi, M., Nitta, S., Tatematsu, Y., & Tomimatsu, A. 1990, ApJ, 363, 206
Takahashi, M., Rilett, D., Fukumura, K., & Tsuruta, S. 2002, ApJ, 572, 950
Yang, R., & Kafatos, M. 1995, A&A, 295, 238
Yuan, F., & Narayan, R. 2014, ARA&A, 52, 529